

<https://doi.org/10.1038/s43247-024-01294-x>

California dominates U.S. emissions of the pesticide and potent greenhouse gas sulfuryl fluoride

Check for updates

Dylan C. Gaeta¹✉, Jens Mühle², Isaac J. Vimont³, Molly Crotwell^{3,4}, Lei Hu³, John B. Miller³, Kathryn McKain³, Bianca C. Baier³, Mingyang Zhang¹, Jianing Bao^{1,5}, Benjamin R. Miller³ & Scot M. Miller¹✉

Sulfuryl fluoride (SO₂F₂) is a synthetic pesticide and a potent greenhouse gas that is accumulating in the global atmosphere. Rising emissions are a concern since SO₂F₂ has a relatively long atmospheric lifetime and a high global warming potential. The U.S. is thought to contribute substantially to global SO₂F₂ emissions, but there is a paucity of information on how emissions of SO₂F₂ are distributed across the U.S., and there is currently no inventory of SO₂F₂ emissions for the U.S. or individual states. Here we provide an atmospheric measurement-based estimate of U.S. SO₂F₂ emissions using high-precision SO₂F₂ measurements from the NOAA Global Greenhouse Gas Reference Network (GGGRN) and a geostatistical inverse model. We find that California has the largest SO₂F₂ emissions among all U.S. states, with the highest emissions from southern coastal California (Los Angeles, Orange, and San Diego counties). Outside of California, only very small and infrequent SO₂F₂ emissions are detected by our analysis of GGGRN data. We find that California emits 60–85% of U.S. SO₂F₂ emissions, at a rate of 0.26 (± 0.10) Gg yr⁻¹. We estimate that emissions of SO₂F₂ from California are equal to 5.5–12% of global SO₂F₂ emissions.

Following the Montreal Protocol on Substances that Deplete the Ozone Layer¹, the use of methyl bromide (CH₃Br) as a fumigant was largely phased out by 2005, with some exemptions for critical and quarantine/pre-shipment (QPS) uses. As a result, the atmospheric abundance of CH₃Br has declined, and the stratospheric ozone layer is showing signs of recovery in recent years due to the phase-out of CH₃Br and other ozone-depleting substances (ODSs)^{2–4}. However, an unintended consequence of the CH₃Br phase-out is that global use of sulfuryl fluoride (SO₂F₂), a non-ODS fumigant alternative to CH₃Br, has dramatically increased^{5,6}. Like CH₃Br, SO₂F₂ is a broad spectrum pesticide used to exterminate structural, commodity, and stored product pests such as drywood termites, subterranean termites, cockroaches, wood-boring beetles, moths, bed bugs, and rodents^{7–9}. While SO₂F₂ is not an ODS, it is a potent greenhouse gas (GHG) that is accumulating in the global atmosphere, with an ambient air mole fraction that has risen from ~0.3 parts per trillion (ppt) in 1978 to nearly 3.0 ppt in 2023^{5,10}.

Recent measurements and global modeling from the Advanced Global Atmospheric Gases Experiment (AGAGE) indicate that global emissions of SO₂F₂ have reached a historic high of nearly 3.0 Gg yr⁻¹, and global mean atmospheric mole fractions of SO₂F₂ have continued to increase at a rate of nearly 0.1 ppt yr⁻¹ (4% yr⁻¹) from 2015 to 2023^{4,5,11}. At present, the effective radiative forcing of SO₂F₂ is small at ~0.5 mW m⁻², but increasing as global mole fractions of SO₂F₂ continue to rise¹². Rising emissions of SO₂F₂ are a concern because SO₂F₂ exhibits strong infrared absorption properties, has a relatively long atmospheric lifetime, and therefore has a high global warming potential (GWP)^{10,12–16}.

When SO₂F₂ was first approved for use as a fumigant/pesticide by regulators in 1959, its atmospheric lifetime was thought to be negligible, and thus the study of its environmental fate was largely neglected^{17,18}. However, seminal studies published in 2008–2009 on the atmospheric chemistry of SO₂F₂ demonstrated that removal of SO₂F₂ from the atmosphere is predominantly mediated by ocean uptake and hydrolysis, resulting in a

¹Department of Environmental Health and Engineering, Johns Hopkins University, Baltimore, MD 21218, USA. ²Scripps Institution of Oceanography, University of California San Diego, La Jolla, CA 92093, USA. ³Global Monitoring Laboratory, National Oceanic and Atmospheric Administration, Boulder, CO 80305, USA.

⁴Cooperative Institute for Research in Environmental Sciences, University of Colorado Boulder, Boulder, CO 80309, USA. ⁵Present address: Department of Environmental Engineering and Earth Sciences, Clemson University, Anderson, SC 29625, USA. ✉e-mail: dgaeta@jhu.edu; smill191@jhu.edu

relatively long effective atmospheric lifetime of 36 (± 11) years^{10,13–15}. Consequentially, the GWP of SO₂F₂ was revised to be much larger than initially thought, recently estimated at 7510 for a 20-year time horizon, or 4630 for a 100-year time horizon^{4,12}. (See Supplementary Note 1 for additional background on SO₂F₂ in the atmosphere). The Intergovernmental Panel on Climate Change (IPCC) characterized SO₂F₂ as a well-mixed GHG with a high GWP in its 2013 Fifth Assessment Report¹⁶. Yet, SO₂F₂ was not included in the 2015 Paris Climate Agreement, nor subsequent international legislation on climate change and GHG emissions under the United Nations Framework Convention on Climate Change (UNFCCC)^{19,20}.

Despite recent advances in scientific knowledge of atmospheric SO₂F₂, no top-down, atmospheric measurement-based estimate of SO₂F₂ emissions exists for the U.S. There is also no national inventory of SO₂F₂ use, and SO₂F₂ is not included in the EPA Greenhouse Gas Reporting Program (GHGRP) or National Greenhouse Gas Inventory (GHGI)^{21,22}. Furthermore, California is the only state that keeps a public record of statewide SO₂F₂ use²³. The lack of inventory data on SO₂F₂ use complicates attempts to constrain U.S.-wide emissions of SO₂F₂²⁴. To address this challenge, we utilize inverse modeling to infer SO₂F₂ emissions directly from high-

precision measurements of atmospheric SO₂F₂ collected across North America throughout 2015–2019. We analyze these measurements using a geostatistical inverse model (GIM) to estimate surface emissions of SO₂F₂ over the continental U.S., and we compare our top-down inverse model estimates with available state records of SO₂F₂ use²³ and recent global emissions rate estimates from AGAGE⁵. Overall, we find that the largest SO₂F₂ emissions are from California, with zero to low emissions across most of the rest of the U.S.

Results and discussion

Atmospheric measurements of SO₂F₂ reveal an unusual pattern

We use measurements of SO₂F₂ from the NOAA Global Monitoring Laboratory (NOAA/GML) Global Greenhouse Gas Reference Network (GGGRN) collected throughout 2015–2019 at sites shown in Fig. 1 as the principal data constraint in our analysis¹¹. Most GGGRN measurements (>90%) show SO₂F₂ mole fractions <5 ppt and are clustered around the global background mole fraction of 2.0–2.5 ppt (Fig. 2a). However, numerous enhancements (10–450 ppt) are also observed throughout the study period (Fig. 2b), 98% of them at sites in California. The vast majority of

Fig. 1 | Map of the mean footprint (sensitivity) of NOAA GGGRN observations to SO₂F₂ emissions. The mean footprint in each grid box is colored by quintile in shades of blue (2015–2019, $N_{\text{obs}} = 15,385$). Quintiles are defined relative to the maximum of the daily mean footprint. Red markers show GGGRN tower/surface sites, yellow markers represent locations of regular NOAA/GML vertical-profiling aircraft sites, and small orange markers indicate locations of individual samples collected during intensive aircraft campaigns.

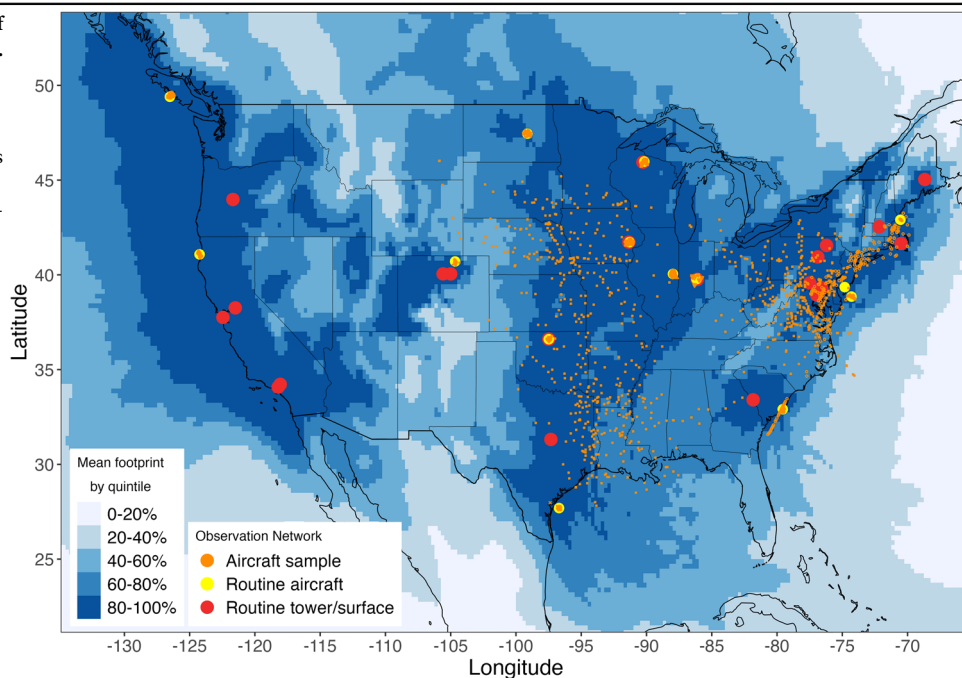


Fig. 2 | Frequency of observed SO₂F₂ mole fractions in NOAA GGGRN measurements, colored by site. Panel (a) shows a frequency histogram of GGGRN observations <5.0 ppt (bin size = 0.25 ppt). Panel (b) shows a frequency histogram of GGGRN observations >10.0 ppt (bin size = 10.0 ppt). The vertical dotted and dashed lines indicate the mean and median observed values, respectively.

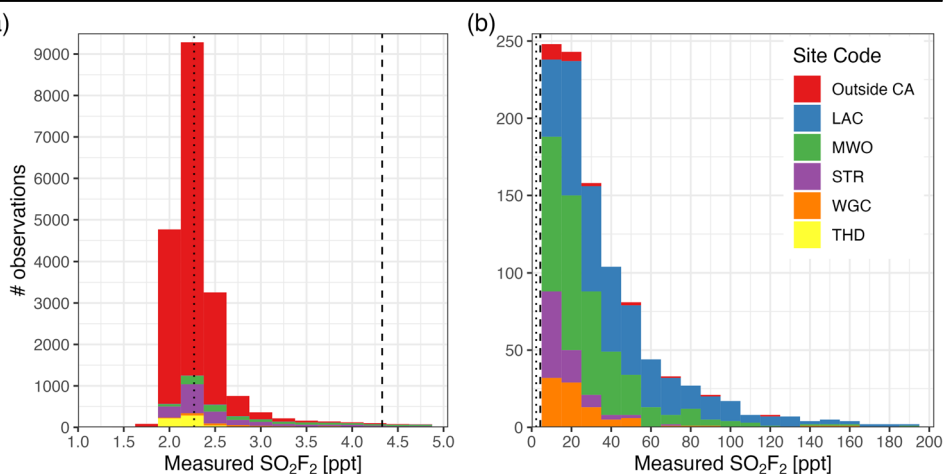
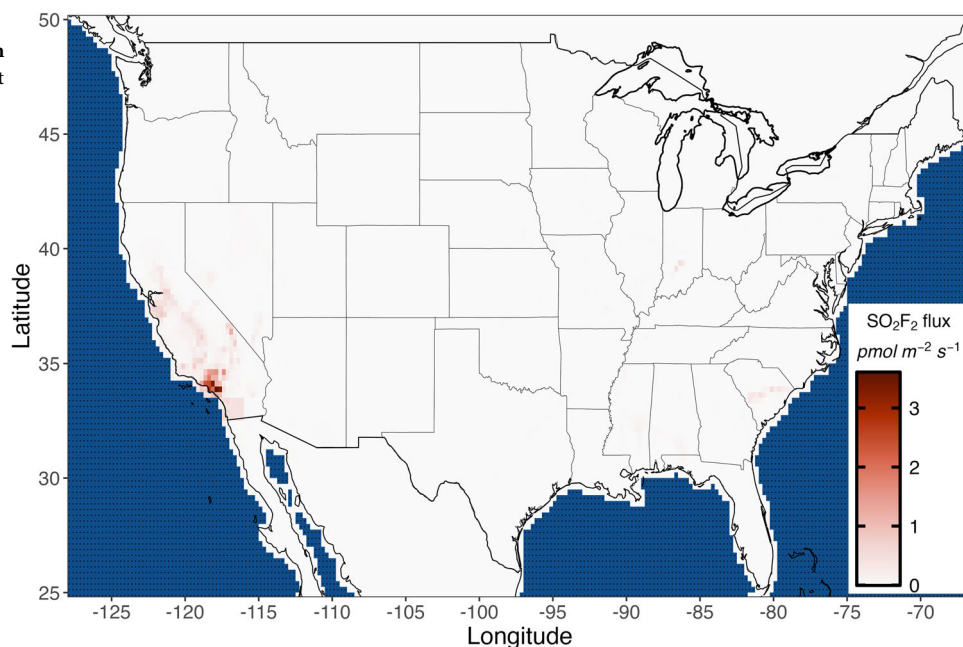


Fig. 3 | GIM estimate of SO₂F₂ emissions across the continental U.S. The largest emissions, shown in red, are from California. Across most of the rest of the U.S., emissions are low to zero and sparse, shown in white.



enhancements (85%) are observed at either the Los Angeles Megacity Carbon Project (LAC) observation sites^{25,26} or the Mt. Wilson Observatory (MWO) in Los Angeles, California²⁷. Notably, measurements at the LAC sites are only available between June 2015 and October 2017 ($N_{\text{days}} = 852$), but measurements at MWO are ongoing¹¹. Numerous SO₂F₂ enhancements are also observed at two other sites in central California (Sutro tower (STR) and Walnut Grove tower (WGC), $N = 117$), while none are observed during aircraft flights at Trinidad Head (THD). For additional details on how these SO₂F₂ enhancements are defined relative to the global background SO₂F₂ mole fraction, see Supplementary Note 3 (Supplementary Figs. 4–7).

Outside of California, SO₂F₂ enhancements occur very infrequently ($N = 16$, $< 1 \text{ yr}^{-1}$) at only a few sites. In addition, no monitoring site outside of California records the frequent (sub-weekly) and large ($> 10 \times$) SO₂F₂ enhancements that are characteristic of the LAC and MWO sites in Los Angeles. However, it is important to note that SO₂F₂ enhancements do not translate linearly to SO₂F₂ emissions, since other factors such as wind direction, wind speed, atmospheric boundary layer height, and the distance between the emissions and the observation site can influence the measured enhancements. While Fig. 2 indicates that the likelihood of large emissions from California is higher than elsewhere, an inverse model is needed to infer the emissions fluxes (and corresponding uncertainties) from the measured enhancements.

We correlate these measured atmospheric mole fractions of SO₂F₂ with estimated surface emissions using an atmospheric transport model. We specifically calculate daily, gridded footprints, which quantitatively describe the potential of upwind locations to influence SO₂F₂ mole fractions at downwind observation sites. These footprints have units of atmospheric SO₂F₂ mole fraction (ppt) per unit emission, and they are a measure of the effective geographic coverage of the observation network. A map of the mean footprint across all GGGRN measurements is shown in Fig. 1 to illustrate the broad spatial coverage of emissions monitoring provided by the GGGRN. The footprint map indicates that if SO₂F₂ emissions occurred within most of the highly-populated regions of the U.S., SO₂F₂ enhancements would be detected by at least one of the GGGRN sites nearby.

Largest U.S. SO₂F₂ emissions are from California

We use a geostatistical inverse model (GIM) to infer surface emissions of SO₂F₂ from the GGGRN atmospheric measurements^{28–30}. The GIM leverages atmospheric observations, coupled with an atmospheric transport model, to interpolate grid-scale SO₂F₂ emissions across the

continental U.S. GIMs have been used widely in the atmospheric science community to estimate trace gas emissions given a set of atmospheric mole fraction measurements e.g.,^{31–36}. Importantly, the GIM also provides a statistical methodology for calculating uncertainties in the estimated emissions^{28,30}.

Our inverse modeling results exhibit a dichotomy between the state of California and the rest of the U.S., shown in Fig. 3. Emissions from California are both large in magnitude and persistent throughout the study period, especially from coastal southern California (Los Angeles, Orange, and San Diego counties). Specifically, we estimate the annual mean SO₂F₂ emissions rate from California at $0.26 (\pm 0.10) \text{ Gg yr}^{-1}$. Uncertainties are reported as 2- σ errors (equivalent to 95% confidence intervals), with errors calculated from the posterior covariance matrix from the GIM²⁹. Posterior uncertainties from the GIM include the aggregate effects of measurement, model, atmospheric transport, representation, and spatial/temporal aggregation errors. For more details on the GIM, see the Methods section and Supplementary Note 4 (and references therein).

We estimate the annual mean emissions rate for the entire continental U.S. at $0.30 (\pm 0.18) \text{ Gg yr}^{-1}$, with the bulk of those emissions (60–85%) coming from California. Outside of California, emissions are small and sparse (Fig. 3), with an annual mean emissions rate of $0.05 (\pm 0.16) \text{ Gg yr}^{-1}$ for all other continental U.S. states combined. For many states with a colder climate, this result may be expected, as the threat from wood-destroying termites and thus the need for structural fumigation with SO₂F₂ is lower outside of the warm coastal regions. However, this result of low emissions for other warm coastal regions, such as the Gulf Coast and the Atlantic Coast, may appear surprising.

While the magnitude of emissions from California is substantially larger than the rest of the U.S., the corresponding uncertainties are smaller for California than for the rest of the U.S., largely due to two main factors. First, emissions totals are summed over a much larger area outside of California, resulting in a larger uncertainty. Second, there is a higher spatial density of observations in California than for most other parts of the U.S., resulting in smaller uncertainties for California and larger uncertainties for regions that are not as densely sampled spatially. The sparsity of the observation network, combined with the ephemeral nature of SO₂F₂ fumigation events, makes SO₂F₂ emissions especially uncertain outside of California. For additional information on the inverse model best estimate of U.S. SO₂F₂ emissions, see Supplementary Note 5 (Supplementary Figs. 11–14).

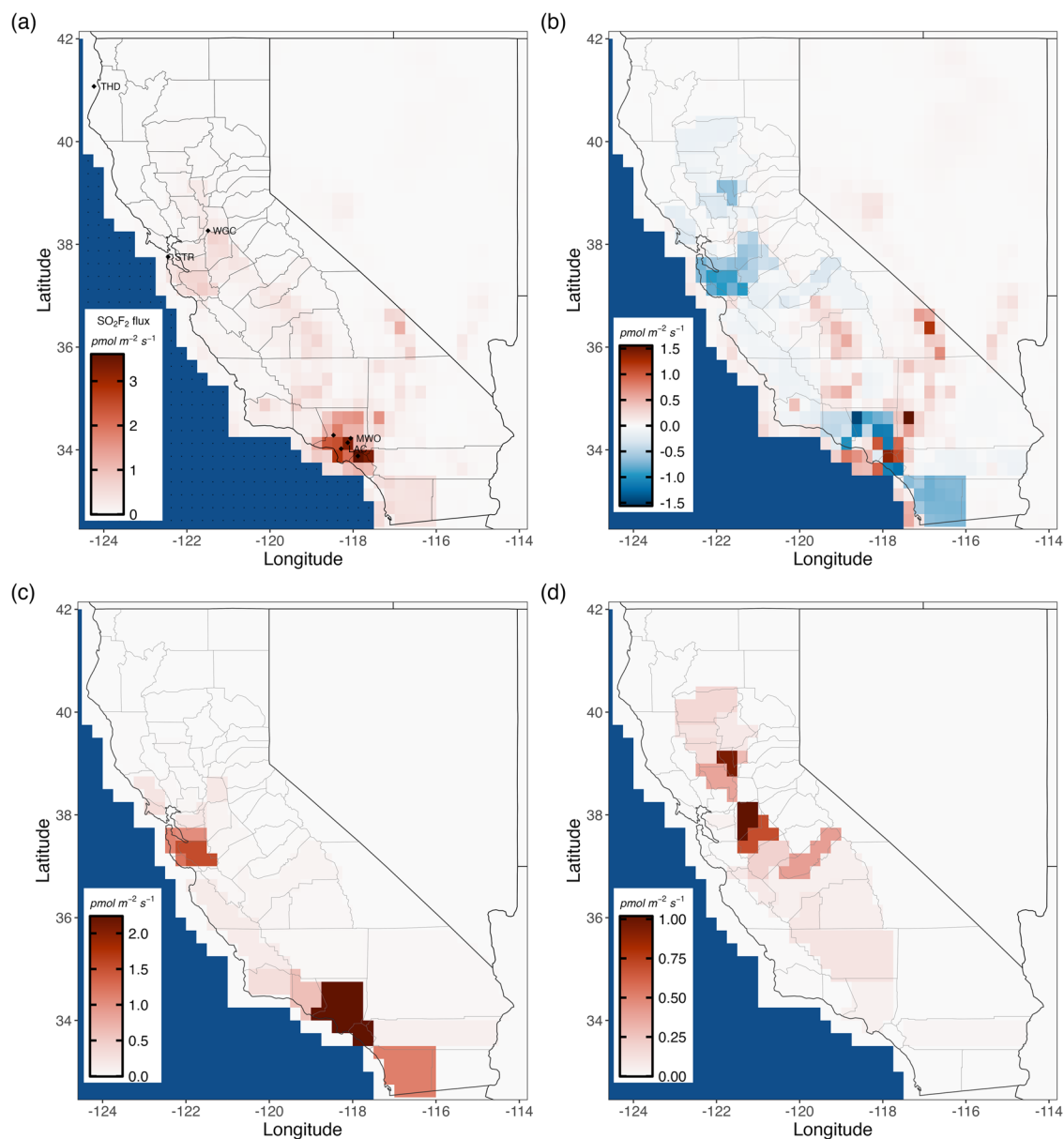


Fig. 4 | Emissions maps showing the relative contribution of the predictor variables and the stochastic variable to the GIM best estimate of emissions in California. Panel (a) shows the GIM best estimate of SO_2F_2 emissions. Panel (b) shows the mean contribution of the stochastic variable. Panel (c) shows the

contribution of the structural fumigation predictor variable only, and Panel (d) shows the contribution of the agricultural/commodity fumigation predictor variable only. The emissions pattern in Panel (a) is a linear combination of the emissions patterns in Panels (b), (c), and (d).

An important caveat of our results is that the GGGRN is not highly sensitive to emissions from Florida (Fig. 1), a state that is at high-risk for termite infestations³⁷, potentially resulting in SO_2F_2 use and emissions^{38,39}. In Supplementary Note 7 (Supplementary Figs. 20–22), we conduct a sensitivity test and find that if daily emissions from Florida were comparable in magnitude to SO_2F_2 emissions from California, those emissions would be regularly detected at the closest tower site in South Carolina (SCT). However, the actual GGGRN measurements at SCT, as well as the ECO flights, show no evidence of SO_2F_2 emissions in all but one sample. While our present work does not rule out sparse and/or infrequent SO_2F_2 emissions from Florida, we find that the annual emissions of SO_2F_2 from California, relative to the southeast U.S., are substantially larger. At the very least, our study underscores the potential utility of adding a long-term GGGRN site in Florida, which would help constrain emissions of GHGs and other natural and anthropogenic trace gases in this otherwise data sparse region of the U.S.

Majority of emissions likely from structural fumigation

State records from the California Department of Pesticide Regulation (CDPR) indicate that ~85% of SO_2F_2 use (by mass) in California is for structural fumigation, while ~15% is for agricultural and commodity fumigation²³. We see a similar end use disparity in our inversion results (Fig. 4).

To help estimate the contribution of these different SO_2F_2 sources, the GIM allows the inclusion of spatially explicit predictor variables^{30,32}. We find that two variables, both defined from CDPR data, are optimal predictor variables: (1) county-level SO_2F_2 use for structural fumigation in California (Fig. 4c) and (2) county-level SO_2F_2 use for agricultural and commodity fumigation in California (Fig. 4d)²³. The CDPR data on SO_2F_2 usage is described in further detail in Supplementary Note 2 (Supplementary Figs. 1–3).

The GIM also includes a stochastic component (Fig. 4b), which is an estimate of spatial and temporal emissions patterns that are not already

described by the predictor variables. By construction, the stochastic variable follows a multivariate normal distribution with a mean of zero⁴⁰. The overall modeled emissions (Fig. 4a) are a linear combination of the predictor variables and the stochastic variable. The stochastic variable and the relative weights on the predictor variables are optimized as parameters in the inverse model to best match the atmospheric observations and are not known a priori.

Figure 4 shows the relative contribution of the predictor variables and the stochastic term to the total emissions in Fig. 3. Consistent with the CDPR inventory, the largest contribution to the emissions totals arises from the predictor variable defined by the CDPR dataset of county-level SO₂F₂ use for structural fumigation. Together, our inversion results and the CDPR inventory imply that structural fumigation (specifically in California) is the predominant source of SO₂F₂ emissions across the U.S.

Note that we examine several other candidate predictor variables, including those with information outside of California, but none of these variables (or any linear combination of them) improve the model-data errors relative to the inversion setup with the optimal variables. For additional details on model selection of predictor variables, see Supplementary Note 4 (Supplementary Figs. 9, 10)⁴⁰. In Supplementary Note 6 (Supplementary Table 3, Supplementary Figs. 15–19), we show additional inverse modeling results using alternative predictor variables to demonstrate that our results are robust across different choices of predictors in the GIM, such as land cover classifications from the National Land Cover Database (NLCD) (agreement within 7% for both U.S. and California emissions)⁴¹. Furthermore, we find that our results are consistent in magnitude and spatial distribution (agreement within 5% for U.S. emissions and within 20% for California emissions) even when we use a spatially uniform prior in the GIM, adding confidence to the spatial pattern in our results.

Reconciling top-down emissions with California state data

Our inverse model results indicate that the largest U.S. SO₂F₂ emissions occur in southern coastal California. This result is consistent with California state records of county-level SO₂F₂ use from the CDPR, which indicate that Los Angeles, Orange, and San Diego counties alone account for >50% of statewide SO₂F₂ use, with Los Angeles County being the largest use county²³.

According to CDPR records²³, SO₂F₂ use in California has been steadily increasing from 0.976 Gg in 2007 to 1.367 Gg in 2018, with a mean statewide use of 1.435 Gg SO₂F₂ yr⁻¹ from 2015–2017. However, our inverse modeling results indicate an annual mean SO₂F₂ emissions rate of only 0.16–0.36 Gg yr⁻¹, equivalent to only 11–25% of the total reported SO₂F₂ use in 2015–2017 (assuming accurate SO₂F₂ usage data reporting to CDPR). This emitted fraction is notably smaller than the previous estimate of ~2/3, which was derived from a comparison between global box model emissions estimates using AGAGE data and an estimate of global industrial SO₂F₂ production¹⁰.

The emitted fraction is important for two main reasons. First, for structural fumigation, the fraction of SO₂F₂ that is not absorbed or destroyed on surfaces during fumigation likely escapes to the atmosphere, contributing to the greenhouse effect¹⁰. Second, for agricultural and commodity fumigation, the absorbed fraction of SO₂F₂ could have implications on the amount of fluoride, sulfate, and other residues that humans and animals are exposed to in their diets^{42,43}.

Comparison with global emissions estimates from AGAGE

Recent work by Gressent et al.⁵ provides an atmospheric measurement-based estimate of global mean SO₂F₂ emissions: ~2.89 Gg yr⁻¹ over 2015–2017⁵. This global emissions rate is likely accurate, as it is based on the increase of global baseline atmospheric measurements of SO₂F₂ assimilated into the AGAGE 12-box model^{10,44}. Neglecting any issues with comparability between AGAGE and NOAA measurements (e.g., calibration standards), our estimate of 0.16–0.36 Gg yr⁻¹ for California accounts for 5.5–12% of global SO₂F₂ emissions.

However, in contrast to our study, regional atmospheric measurements were not used in Gressent et al.⁵. This resulted in an estimate of large down-

scaled SO₂F₂ emissions throughout the central and eastern U.S., a scenario not observed in the regional GGGRN measurements or our inverse model estimates. Gressent et al.⁵ used a proxy-based estimate to define the spatial pattern of SO₂F₂ emissions, constructed as the sum of (1) a structural fumigation component, which scales with population density (multiplied by a binary mask indicating whether or not a region has termites), and (2) a post-harvest treatment component, which scales with cropland fraction. In our work, however, we find that neither crop cover fraction nor population density are skilled predictor variables of regional atmospheric measurements outside of California. The use of these variables by Gressent et al.⁵ to define the spatial pattern of U.S. SO₂F₂ emissions likely overestimates emissions for most agricultural regions and densely populated areas outside of California. It is also likely that these variables do not predict SO₂F₂ use in colder regions of the U.S. with lower termite risk.

California faces challenges with drywood termites

While subterranean termites are pervasive across most of the U.S., California is home to a challenging termite species that helps explain the abundance of SO₂F₂ fumigation in the state: the western drywood termite, *Incisitermes minor* (Hagen) (*I. minor*)^{8,9}. Drywood termites are particularly difficult to treat because they establish colonies without having contact with the soil⁹. Effective fumigant-free methods that utilize bait are available for treating subterranean termites^{45,46}, but these methods are ineffective against drywood termites, which do not forage for their food. Furthermore, *I. minor* (and other drywood termites, such as the West Indian drywood termite *Cryptotermes brevis* (Walker)) form aerial colonies in high, inaccessible parts of wooden structures, leading to situations where fumigation is the most effective eradication method⁹.

Notably, SO₂F₂ fumigation does not provide residual protection against future infestations, prompting reoccurring treatments of structures situated in regions with pervasive termites⁹. Alternatively, several non-fumigation treatment methods exist, including localized treatments such as wood replacement, wood injection with pesticides, hot (>50°C) and cold (liquid nitrogen) temperature treatments, electrocution, and microwave radiation^{8,9}. However, these alternative methods generally do not provide whole-structure eradication of termites. The pervasive threat of termite infestations in warm-climate regions highlights the need for the development and practice of sustainable, entomology-guided techniques for controlling urban pest populations without the release of harmful atmospheric pollutants or climate-warming gases^{8,9,45}.

Significance and policy relevance

California's SO₂F₂ emissions provide a case study on how greenhouse gas emissions that are unaccounted for in emissions inventories can potentially offset progress made towards emissions reductions. In 2006, California passed AB-32, the Global Warming Solutions Act⁴⁷, which charged the California Air Resources Board (CARB) with monitoring and regulating statewide emissions sources of GHGs, and set a target of reducing statewide GHG emissions to 1990 levels by 2020. However, since the long atmospheric lifetime of SO₂F₂ was not discovered until 2009, SO₂F₂ was not included in AB-32. California renewed its commitment to emissions reductions in 2016 by passing SB-32, which expanded upon AB-32 and set a statewide GHG emissions reduction target of 40% below 1990 levels by 2030⁴⁸. Although CARB classified SO₂F₂ as a short-lived climate pollutant (SLCP) in 2016, it has yet to add the gas to the state's annual GHG emissions inventory or its latest Climate Change Scoping Plan^{49,50}.

From 2007–2019, California reports an average of 4.8 Tg CO₂ equivalents (CO₂e) yr⁻¹ in statewide GHG emissions reductions under AB-32¹⁹. (1 Tg = 1 million metric tons (MMT)). Notably, these emissions reductions slowed and plateaued to an average of 2.25 Tg CO₂e yr⁻¹ from 2010–2015. Our inverse model results imply an annual mean SO₂F₂ emissions rate of 0.7–1.7 Tg CO₂e yr⁻¹ (100-yr GWP) or 1.2–2.7 Tg CO₂e yr⁻¹ (20-yr GWP) for 2015–2017²³. Thus, the short-term warming effect of California's annual SO₂F₂ emissions, which are unaccounted for under California's current GHG accounting protocol, are smaller yet comparable

in scale to the annual statewide CO₂e reductions achieved under AB-32. In other words, California could accelerate its future GHG emissions reductions by including SO₂F₂ in GHG emissions inventories and phasing out the use of SO₂F₂ in the state, and/or mandating abatement of SO₂F₂ emissions.

SO₂F₂ is also regulated in the U.S. by the Environmental Protection Agency (EPA) as a restricted-use pesticide (RUP) due to its inhalation toxicity^{17,18,43,51–54}, and is currently undergoing re-registration review by the EPA⁵⁵. SO₂F₂ is the only fumigant approved by the EPA for structural fumigation, and it is one of several options available for agricultural and commodity fumigation.

Apart from the climate-warming effect, there are public health and safety concerns surrounding the use of SO₂F₂ for fumigation. Most notably, there have been several documented cases of inadvertent human deaths caused by acute exposure to SO₂F₂, and numerous human health and safety concerns have been reported^{42,43,51–57}. The EPA has set a human exposure limit of 1 part per million (ppm) SO₂F₂, which is the clearance level for reoccupation of a fumigated structure⁵⁵. As indoor SO₂F₂ levels during fumigation typically exceed 1,000 ppm, ambient air levels around fumigation sites could potentially exceed the 1 ppm exposure limit. Aeration of fumigated structures has been demonstrated to occur rapidly, with over 90% of indoor SO₂F₂ lost to the atmosphere within the first 2 hours of ventilation^{58,59}. Recent aerial thermal-IR spectral imaging surveys over the Los Angeles Basin have identified SO₂F₂ emissions plumes emanating from fumigation sites in residential neighborhoods^{60,61}. Under the Clean Air Act⁶², the EPA is required to regulate emissions of hazardous air pollutants (HAPs), but SO₂F₂ has not been included in the list of HAPs to date.

Potential solutions

There are potentially steps that fumigators and fumigation regulators can investigate to minimize the amount of SO₂F₂ that escapes to the atmosphere during structural fumigation procedures. For example, strong basic solutions and bio-based organic solvents have been shown to effectively absorb and destroy SO₂F₂^{63–66}. These SO₂F₂ chemical absorption methods could be utilized at the exhaust vents of fumigated structures to capture SO₂F₂ and prevent its escape to the atmosphere. Implementing an SO₂F₂ capture step in the post-fumigation venting process could result in GHG emissions reductions on the order of 1–3 Tg CO₂e, while also minimizing the risk of SO₂F₂ exposure to nearby residents and fumigation workers.

A fumigant re-capture step may increase the upfront cost of fumigation, but doing so would also provide the global climate and environmental benefits of reducing SO₂F₂ emissions. However, further work is required to reduce the cost and technical barriers to these solutions. Nevertheless, the process of emitting SO₂F₂ directly to the atmosphere after fumigation, as is standard practice under the California Aeration Plan⁵⁹, leads to a previously under-emphasized climate warming effect, and could potentially be reconsidered as an option for achieving future GHG emissions reductions.

Methods

Atmospheric measurements of SO₂F₂

We use atmospheric measurements of SO₂F₂ from the NOAA Global Monitoring Laboratory (NOAA/GML) Global Greenhouse Gas Reference Network (GGGRN)¹¹. NOAA/GML began measuring SO₂F₂ in air samples collected at sites shown in Fig. 1 in 2015. Air samples were collected via programmable flask packages (PFPs) at surface and tower sites, from vertical-profiling NOAA/GML aircraft flights, and during the Atmospheric Carbon and Transport - America (ACT) and the East Coast Outflow (ECO) aircraft campaigns^{67–71}. High-precision measurements of the SO₂F₂ mole fraction in each PFP collected from these measurement platforms were made by NOAA/GML on the PERSEUS-1 gas chromatography/mass spectrometry (GC-MS) instrument. These measurements are quite accurate, with a mean measurement error of <0.05 ppt (within 2% of the ~2.5 ppt background). In total, we include $N = 15,385$ measurements of SO₂F₂ in our analysis (10,157 from towers and surface observatories, 5,228 from aircraft). For additional details on the NOAA/GML measurements of

SO₂F₂, see Supplementary Note 3 (Supplementary Figs. 4–8 and Supplementary Tables 1 and 2).

Atmospheric transport model (STILT)

We use an atmospheric transport model to correlate measured atmospheric mole fractions of SO₂F₂ (z) with daily grid-scale surface emissions (s). Specifically, we employ the Stochastic Time-Inverted Lagrangian Transport (STILT) model with atmospheric wind fields defined by the North American Mesoscale Forecast System 12-km resolution meteorology data (NAM-12)^{72–76}. We use NAM-STILT to quantitatively model SO₂F₂ mole fractions in the atmosphere given a map of estimated SO₂F₂ emissions. Using this transport model and the GIM, we optimize the emissions maps such that our modeled SO₂F₂ mole fractions match observations.

We use STILT to simulate the transport of an ensemble of theoretical particles released at the time and location of a given measurement backward in time in order to quantify the sensitivity of that measurement to upwind surface emissions. Particle ensembles are initialized at the time, latitude, longitude, and altitude of each measurement, and transported backwards in time at hourly time steps, with transport probabilities inferred from the NAM-12 meteorology fields.

We run STILT once for each of the 15,385 SO₂F₂ observations used in this study, and each simulation is run 10 days back in time to ensure that the trajectories reach the edge of the regional modeling domain. We then integrate these back-trajectories over time and volume to calculate surface influence footprints (units: ppt SO₂F₂ per unit emission flux), which quantify the influence of grid-scale surface fluxes on each SO₂F₂ measurement.

Each footprint defines the sensitivity of an individual measurement to emissions at different locations (throughout the modeling domain) and times (up to 10 days prior to the measurement). Footprints have units of ppt SO₂F₂ per pmol m⁻² s⁻¹ (mole fraction SO₂F₂ per unit surface flux), gridded at 0.25° × 0.25° latitude-longitude resolution. We estimate SO₂F₂ emissions at a daily time scale in this study, so we calculate footprints at a daily time resolution (yielding 10 daily footprints for each SO₂F₂ measurement). These daily footprints are then used as an input in the GIM.

Geostatistical Inverse Model

We utilize a geostatistical inverse model (GIM) to infer surface fluxes of SO₂F₂ (s) from atmospheric measurements (z)^{28,30,36}. For additional examples of studies that use GIMs to estimate trace gas emissions, see the following references^{30–32,34,36,77–79}.

The NOAA GGGRN measurements of SO₂F₂ are the principal data constraint in our model. These observations z (dimensions $n \times 1$) are modeled as:

$$z = \mathbf{H}s + \boldsymbol{\varepsilon} \quad (1)$$

In our notation here, we use bold fonts to denote matrices, and bold italicized font to denote vectors. In Eq. (1), \mathbf{H} (dimensions $n \times m$) is a sensitivity matrix describing correlations between measured SO₂F₂ mole fractions and modeled surface emissions (i.e. $\mathbf{H}_{i,j} = \partial z_i / \partial s_j$), defined by the STILT footprints (discussed above and in the main text). s (dimensions $m \times 1$) are the unknown surface emissions for each model grid box on each day of the time series ($m = N_{\text{days}} \cdot N_{\text{lat}} \cdot N_{\text{lon}}$). The variable $\boldsymbol{\varepsilon}$ (dimensions $n \times 1$) is a vector of the model-data residuals, which include the aggregate effects of measurement error, transport error, representation error, and aggregation error. By construction, $\boldsymbol{\varepsilon}$ is distributed as a multivariate normal distribution $\mathcal{N}(0, \mathbf{R})$ with a mean of zero and covariances defined by the matrix \mathbf{R} .

The covariance matrix \mathbf{R} (dimensions $n \times n$) describes the expected magnitude of model-data errors due to measurement, transport, representation, and aggregation.

$$\mathbf{R} = E[\boldsymbol{\varepsilon}] = E[(z - \mathbf{H}s)(z - \mathbf{H}s)^T] \quad (2)$$

Here, $E[\cdot]$ indicates the expected value of a variable and T indicates the matrix transpose. In general, \mathbf{R} can be thought of as a control on how precisely $\mathbf{H}\mathbf{s}$ must match the atmospheric measurements \mathbf{z} . Notably, there are tradeoffs associated with different configurations of \mathbf{R} . For instance, using a value for σ_R that is too small runs the risk of overfitting the data, while using a value for σ_R that is too large can lead to model estimates that do not adequately reproduce the measurements. In this study, we construct \mathbf{R} as a diagonal matrix, with diagonal elements σ_R^2 . The off-diagonal elements of \mathbf{R} describe spatial and temporal covariances in the emissions, which we assume to be zero in this study since SO_2F_2 emissions are transient and arise rapidly from non-stationary point sources^{58,61}.

We run case studies using both a uniform value for the diagonal elements of \mathbf{R} and a non-uniform setup where the diagonal elements vary by measurement site, proportional to the observed variance in the enhancements at each site³⁰. The results of this sensitivity study are shown in Supplementary Note 6 (Supplementary Table 3 and Supplementary Figs. 15–19), and demonstrate that the resulting emissions pattern is not very sensitive to whether \mathbf{R} is constructed as a scalar matrix defined by a single parameter or as a diagonal matrix with elements that vary by measurement site. Using an \mathbf{R} matrix with covariances that vary by measurement site often results in a more realistic quantification of uncertainties associated with different measurement sites, but the tradeoff is that doing so risks over-parameterizing the GIM. We include these case studies to show that our inverse modeling results are not highly dependent on the definition of \mathbf{R} used in the inversion results presented in this study.

The unknown surface emissions \mathbf{s} are modeled as the sum of a deterministic term ($\mathbf{X}\boldsymbol{\beta}$) and a stochastic term $\boldsymbol{\xi}$ (dimensions $m \times 1$)^{36,81}:

$$\mathbf{s} = \mathbf{X}\boldsymbol{\beta} + \boldsymbol{\xi} \quad (3)$$

The deterministic term is defined by the matrix \mathbf{X} (dimensions $m \times p$), which includes p predictor variables, or covariate datasets, that help describe spatial patterns in the estimated fluxes, along with unknown corresponding weights $\boldsymbol{\beta}$ (dimensions $p \times 1$). The deterministic term can be thought of as a weighted linear combination of different spatial datasets that define our inversion prior. The stochastic term $\boldsymbol{\xi}$, by contrast, describes grid-scale patterns in the modeled fluxes that are not adequately described by the explanatory variables in \mathbf{X} . By construction, $\boldsymbol{\xi}$ is distributed as a multivariate normal distribution $\mathcal{N}(0, \mathbf{Q})$ with a mean of zero and covariance matrix \mathbf{Q} (dimensions $m \times m$). Both $\boldsymbol{\xi}$ and $\boldsymbol{\beta}$, and therefore \mathbf{s} , are not known a priori and optimized in the inversion.

Similarly to \mathbf{R} , the flux deviation matrix \mathbf{Q} characterizes how much the estimated emissions \mathbf{s} deviate from the deterministic model:

$$\mathbf{Q} = E[\boldsymbol{\xi}\boldsymbol{\xi}^T] = E\left[(\mathbf{s} - \mathbf{X}\boldsymbol{\beta})(\mathbf{s} - \mathbf{X}\boldsymbol{\beta})^T\right] \quad (4)$$

We assume that deviations of \mathbf{s} from the deterministic model are uncorrelated, and so \mathbf{Q} can be constructed as a diagonal matrix with diagonal elements σ_Q^2 . The off-diagonal elements of \mathbf{Q} represent spatial covariances in the emissions, which we assume to be zero in this study since SO_2F_2 emissions events typically occur rapidly from non-stationary point sources^{58,61}.

The geostatistical approach to solving the inverse problem requires a formulation of the maximum-likelihood posterior emissions distribution. Following Bayes' Theorem on conditional probabilities, the posterior probability distribution of the unknown surface emissions conditional on the atmospheric measurements $p(\mathbf{s}, \boldsymbol{\beta}|\mathbf{z})$ can be written as

$$p(\mathbf{s}, \boldsymbol{\beta}|\mathbf{z}) \propto p(\mathbf{z}|\mathbf{s}, \boldsymbol{\beta})p(\mathbf{s}|\boldsymbol{\beta})p(\boldsymbol{\beta}) \quad (5)$$

The symbol \propto here means “is proportional to.” The first term in Eq. (5), the probability distribution of the atmospheric measurements conditional on

the surface emissions ($p(\mathbf{z}|\mathbf{s}, \boldsymbol{\beta})$), can be derived from Eqs. (1) and (2):

$$p(\mathbf{z}|\mathbf{s}, \boldsymbol{\beta}) \propto \exp\left(-\frac{1}{2}(\mathbf{z} - \mathbf{H}\mathbf{s})^T \mathbf{R}^{-1}(\mathbf{z} - \mathbf{H}\mathbf{s})\right) \quad (6)$$

The second term in Eq. (5), the probability distribution of the surface emissions conditional on the coefficients ($p(\mathbf{s}|\boldsymbol{\beta})$), can be derived from Eqs. (3) and (4):

$$p(\mathbf{s}|\boldsymbol{\beta}) \propto \exp\left(-\frac{1}{2}(\mathbf{s} - \mathbf{X}\boldsymbol{\beta})^T \mathbf{Q}^{-1}(\mathbf{s} - \mathbf{X}\boldsymbol{\beta})\right) \quad (7)$$

As in previous GIM studies, we assume the probability distribution of $\boldsymbol{\beta}$ is uniform across all values:

$$p(\boldsymbol{\beta}) \propto 1 \quad (8)$$

Thus, Eq. (5) can be rewritten as

$$p(\mathbf{s}, \boldsymbol{\beta}|\mathbf{z}) \propto \exp\left(-\frac{1}{2}(\mathbf{z} - \mathbf{H}\mathbf{s})^T \mathbf{R}^{-1}(\mathbf{z} - \mathbf{H}\mathbf{s}) - \frac{1}{2}(\mathbf{s} - \mathbf{X}\boldsymbol{\beta})^T \mathbf{Q}^{-1}(\mathbf{s} - \mathbf{X}\boldsymbol{\beta})\right) \quad (9)$$

The best estimate of the unknown emissions $\hat{\mathbf{s}}$ can be obtained by maximizing the posterior probability distribution $p(\mathbf{s}, \boldsymbol{\beta}|\mathbf{z})$ in Eq. (9). Equivalently, one can minimize the negative logarithm of $p(\mathbf{s}, \boldsymbol{\beta}|\mathbf{z})$, which yields the cost function $L_{s,\beta}$ ^{30,36}:

$$L_{s,\beta} = \frac{1}{2}(\mathbf{z} - \mathbf{H}\mathbf{s})^T \mathbf{R}^{-1}(\mathbf{z} - \mathbf{H}\mathbf{s}) + \frac{1}{2}(\mathbf{s} - \mathbf{X}\boldsymbol{\beta})^T \mathbf{Q}^{-1}(\mathbf{s} - \mathbf{X}\boldsymbol{\beta}) \quad (10)$$

The best estimate of the modeled fluxes $\hat{\mathbf{s}}$ and corresponding regression coefficients $\hat{\boldsymbol{\beta}}$ are obtained by minimizing Eq. (10). We minimize the cost function $L_{s,\beta}$ by taking its derivative with respect to \mathbf{s} and $\boldsymbol{\beta}$ and setting each derivative equal to zero. Numerous methods have been utilized for obtaining $\hat{\mathbf{s}}$ computationally, but in this study we follow the direct approach described by Miller et al. (2020) and preceding work^{30,36,82}. Instead of solving the linear equations for $\hat{\mathbf{s}}$ and $\hat{\boldsymbol{\beta}}$ directly, we can simplify these equations by introducing an unknown vector of weights $\boldsymbol{\zeta}$ (dimensions $n \times 1$):

$$\hat{\mathbf{s}} = \mathbf{X}\boldsymbol{\beta} + \mathbf{Q}\mathbf{H}^T \boldsymbol{\zeta} \quad (11)$$

The unknown vector $\boldsymbol{\zeta}$ and the unknown regression coefficients $\boldsymbol{\beta}$ can then be obtained simultaneously by solving the following linear system of equations:

$$\begin{bmatrix} \mathbf{H}\mathbf{Q}\mathbf{H}^T + \mathbf{R} & \mathbf{H}\mathbf{X} \\ (\mathbf{H}\mathbf{X})^T & 0 \end{bmatrix} \begin{bmatrix} \boldsymbol{\zeta} \\ \boldsymbol{\beta} \end{bmatrix} = \begin{bmatrix} \mathbf{z} \\ \mathbf{0} \end{bmatrix} \quad (12)$$

After solving for $\boldsymbol{\beta}$ and $\boldsymbol{\zeta}$, one can compute $\hat{\mathbf{s}}$ directly by substituting these terms into Eq. (11).

Computing model errors

We follow the methodology described in Kitanidis et al. (1996) for calculating posterior uncertainties (\mathbf{V}_s) corresponding to the best estimate solution to the geostatistical inverse problem ($\hat{\mathbf{s}}$)^{29,83}.

$$\mathbf{V}_s = \mathbf{Q} - (\mathbf{H}\mathbf{Q})^T \mathbf{P}(\mathbf{H}\mathbf{Q}) - \mathbf{X}\mathbf{B}\mathbf{X}^T - \mathbf{X}\mathbf{A}^T(\mathbf{H}\mathbf{Q}) - \mathbf{H}\mathbf{Q}^T \mathbf{A}\mathbf{X}^T \quad (13)$$

The unknown matrices \mathbf{P} , \mathbf{A} , and \mathbf{B} are all computed by inverting the following matrix, as described in Kitanidis et al. (1996)²⁹:

$$\begin{bmatrix} \mathbf{H}\mathbf{Q}\mathbf{H}^T + \mathbf{R} & \mathbf{H}\mathbf{X} \\ (\mathbf{H}\mathbf{X})^T & 0 \end{bmatrix}^{-1} = \begin{bmatrix} \mathbf{P} & \mathbf{A} \\ \mathbf{A}^T & \mathbf{B} \end{bmatrix} \quad (14)$$

After solving for **P**, **A**, and **B**, the posterior uncertainties V_s can be computed directly using Eq. (13). As the daily grid-scale errors can be quite large, we report emissions and corresponding uncertainties summed over a multi-year time interval and over large geographic regions. Previous work has shown that uncertainties decrease exponentially when aggregated over time and space^{34,35}. Thus, in this work we report emissions and uncertainties for three large regions of the U.S.: (1) California only, (2) All continental U.S. states except California, and (3) All continental U.S. states. With respect to time, we report emissions and uncertainties as multi-year averages (2015–2017 for inversions including LAC tower data, and 2015–2019 for inversions including MWO data).

Data availability

Data for the NOAA/GML measurements of SO₂F₂ are available at the data repository maintained by NOAA Global Monitoring Laboratory: <https://doi.org/10.15138/dph1-f551> (specifically, at: https://gml.noaa.gov/aftp/data/trace_gases/so2f2/pfp/)¹¹. California State data on SO₂F₂ use is available via the California Pesticide Information Portal (CalPIP) <https://calpip.cdpr.ca.gov> (specifically, at: https://files.cdpr.ca.gov/pub/outgoing/pur_archives/)²³. NAM-12 meteorology data is available via the NOAA National Centers for Environmental Information at <https://www.ncei.noaa.gov/metadata/geoportal/rest/metadata/item/gov.noaa.ncdc:C00630/html> (specifically, at: <https://www.ncei.noaa.gov/data/north-american-mesoscale-model/>)⁷³.

Code availability

The geostatistical inverse modeling code used in this study is available on Github at https://github.com/greenhousegaslab/geostatistical_inverse_modeling (<https://doi.org/10.5281/zenodo.3241524>) courtesy of Miller and Saibaba (2020)³⁶. The source code for the STILT model is available on Github at <https://uataq.github.io/stilt/>^{72,75}.

Received: 8 September 2023; Accepted: 28 February 2024;

Published online: 03 April 2024

References

- United Nations Environment Programme. Montreal Protocol on Substances that Deplete the Ozone Layer. <https://ozone.unep.org/treaties/montreal-protocol> (1987).
- Yagi, K., Williams, J., Wang, N. Y. & Cicerone, R. J. Atmospheric methyl bromide (CH₃Br) from agricultural soil fumigations. *Science* **267**, 1979–1981 (1995).
- Montzka, S. A., Butler, J. H., Hall, B. D., Mondeel, D. J. & Elkins, J. W. A decline in tropospheric organic bromine. *Geophys. Res. Lett.* **30** (2003).
- World Meteorological Organization. Executive Summary. Scientific Assessment of Ozone Depletion: 2022, GAW Report No. 278. <https://www.unep.org/resources/publication/scientific-assessment-ozone-layer-depletion-2022> (2022).
- Gressent, A. et al. Growing atmospheric emissions of sulfuranyl fluoride. *J. Geophys. Res.: Atmos.* **126**, e2020JD034327 (2021).
- Yu, D. et al. Atmospheric mixing ratios and emissions of sulfuranyl fluoride (SO₂F₂) in China. *SSRN Electron. J.* : <https://www.sciencedirect.com/science/article/pii/S0169809522002083> (2022).
- Derrick, M. R., Burgess, H. D., Baker, M. T. & Binnie, N. E. Sulfuryl fluoride (Vikane): a review of its use as a fumigant. *J. Am. Inst. Conservation* **29**, 77–90 (1990).
- Lewis, V. R. & Haverty, M. I. Evaluation of six techniques for control of the Western Drywood termite (Isoptera: Kalotermitidae) in structures. *J. Econom. Entomol.* **89**, 922–934 (1996).
- Lewis, V. R. & Forschler, B. *Management of Drywood Termites: Past Practices, Present Situation and Future Prospects* <https://doi.org/10.1079/9781780642758.0130> (2014).
- Mühle, J. et al. Sulfuryl fluoride in the global atmosphere. *J. Geophys. Res.* **114**, D05306 (2009).
- Vimont, I. et al. Atmospheric dry air mole fractions of SO₂F₂ from the NOAA GML surface and aircraft vertical profile network. [Data Set]. <https://doi.org/10.15138/dph1-f551> (2023).
- Masson-Delmotte, V. et al. Climate Change 2021: The Physical Science Basis. Working Group I contribution to the Sixth Assessment Report of the Intergovernmental Panel on Climate Change. *IPCC* <https://www.ipcc.ch/report/sixth-assessment-report-working-group-i/> (2021).
- Papadimitriou, V. C. et al. Experimental and theoretical study of the atmospheric chemistry and global warming potential of SO₂F₂. *J. Phys. Chem. A* **112**, 12657–12666 (2008).
- Dillon, T. J., Horowitz, A. & Crowley, J. N. The atmospheric chemistry of sulphuryl fluoride, SO₂F₂. *Atmos. Chem. Phys.* **8**, 1547–1557 (2008).
- Andersen, M. P. S., Blake, D. R., Rowland, F. S., Hurley, M. D. & Wallington, T. J. Atmospheric chemistry of sulfuranyl fluoride: reaction with OH radicals, Cl atoms and O₃, atmospheric lifetime, IR spectrum, and global warming potential. *Environ. Sci. Technol.* **43**, 1067–1070 (2009).
- Myhre, G. et al. Climate Change 2013: The Physical Science Basis. Contribution of Working Group I to the Fifth Assessment Report of the Intergovernmental Panel on Climate Change. *IPCC* (2013).
- United States Environmental Protection Agency. Reregistration Eligibility Decision (RED) Facts Sulfuryl Fluoride. https://www3.epa.gov/pesticides/chem_search/reg_actions/reregistration/fs_PC-078003_1-Sep-93.pdf (1993).
- United States Environmental Protection Agency. Acute Exposure Guideline Levels (AEGLs) for Sulfuryl Fluoride 2699-79-8 Interim. <https://www.epa.gov/aegl/sulfuryl-fluoride-results-aegl-program> (2008).
- United Nations Framework Convention on Climate Change. The Paris Agreement. <https://unfccc.int/documents/184656> (2016).
- United Nations General Assembly. United Nations Framework Convention on Climate Change. <https://digitallibrary.un.org/record/180257> (1994).
- United States Environmental Protection Agency Office of Atmospheric Protection. Greenhouse Gas Reporting Program (GHGRP) <https://www.epa.gov/ghgreporting> (2021).
- United States Environmental Protection Agency. EPA (2022) Inventory of U.S. Greenhouse Gas Emissions and Sinks: 1990-2020 <https://www.epa.gov/ghgemissions/draft-inventory-us-greenhouse-gas-emissions-and-sinks-1990-2020> (2022).
- California Department of Pesticide Regulation. California Pesticide Information Portal (CalPIP) <https://calpip.cdpr.ca.gov/> (2022).
- Gallagher, G. et al. High-global warming potential F-gas emissions in California: comparison of ambient-based versus inventory-based emission estimates, and implications of refined estimates. *Environ. Sci. Technol.* **48**, 1084–1093 (2014).
- Verhulst, K. R. et al. Carbon dioxide and methane measurements from the Los Angeles Megacity Carbon Project—Part 1: calibration, urban enhancements, and uncertainty estimates. *Atmos. Chem. Phys.* **17**, 8313–8341 (2017).
- Miller, J. B. et al. Large and seasonally varying biospheric CO₂ fluxes in the Los Angeles megacity revealed by atmospheric radiocarbon. *Proc. Natl Acad. Sci.* **117**, 26681–26687 (2020).
- Feng, S. et al. Los Angeles megacity: a high-resolution land-atmosphere modelling system for urban CO₂ emissions. *Atmos. Chem. Phys.* **16**, 9019–9045 (2016).
- Kitanidis, P. K. & Vomvoris, E. G. A geostatistical approach to the inverse problem in groundwater modeling (steady state) and one-dimensional simulations. *Water Resour. Res.* **19**, 677–690 (1983).
- Kitanidis, P. K. Analytical expressions of conditional mean, covariance, and sample functions in geostatistics. *Stochastic Hydrol. Hydraulics* **10**, 279–294 (1996).

30. Michalak, A. M. A geostatistical approach to surface flux estimation of atmospheric trace gases. *J. Geophys. Res.* **109**, D14109 (2004).
31. Mueller, K. L., Gourdj, S. M. & Michalak, A. M. Global monthly averaged CO₂ fluxes recovered using a geostatistical inverse modeling approach: 1. Results using atmospheric measurements. *J. Geophys. Res.* **113**, D21114 (2008).
32. Gourdj, S. M., Mueller, K. L., Schaefer, K. & Michalak, A. M. Global monthly averaged CO₂ fluxes recovered using a geostatistical inverse modeling approach: 2. Results including auxiliary environmental data. *J. Geophys. Res.* **113**, D21115 (2008).
33. Gourdj, S. M. et al. North American CO₂ exchange: inter-comparison of modeled estimates with results from a fine-scale atmospheric inversion. *Biogeosciences* **9**, 457–475 (2012).
34. Miller, S. M. et al. Anthropogenic emissions of methane in the United States. *Proc. Natl Acad. Sci.* **110**, 20018–20022 (2013).
35. Miller, S. M. et al. China's coal mine methane regulations have not curbed growing emissions. *Nat. Commun.* **10**, 303 (2019).
36. Miller, S. M., Saibaba, A. K., Trudeau, M. E., Mountain, M. E. & Andrews, A. E. Geostatistical inverse modeling with very large datasets: an example from the Orbiting Carbon Observatory 2 (OCO-2) satellite. *Geosci. Model Dev.* **13**, 1771–1785 (2020).
37. Chouvinc, T., Scheffrahn, R. H. & Buss, L. Termite Species Distribution in Florida and UF Termite Identification Services. *UF/IFAS EDIS* <https://doi.org/10.32473/edis-in1360-2022> (2022).
38. Chouvinc, T., Thoms, E., Brantley, S. & Kern, W. H. 2021 Florida fumigation manual. <https://frec.ifas.ufl.edu/florida-fumigation-manual/> (2021).
39. Scheffrahn, R. H., Mangold, J. R. & Su, N.-Y. A survey of structure-infesting termites of Peninsular Florida. *Florida Entomologist* **71**, 615 (1988).
40. Schwarz, G. Estimating the dimension of a model. *Ann. Statistics* **6**, 461–464 (1978).
41. Dewitz, J. National Land Cover Database (NLCD) 2016 Land Cover Science Product. <https://doi.org/10.5066/P96HHBIE> (2019).
42. Scheffrahn, R. H., Hsu, R. C., Osbrink, W. L. A. & Su, N. Y. Fluoride and sulfate residues in foods fumigated with sulfuryl fluoride. *J. Agric. Food Chem.* **37**, 203–206 (1989).
43. Tsai, W.-T. Environmental and health risks of sulfuryl fluoride, a fumigant replacement for methyl bromide. *J. Environ. Sci. Health C* **28**, 125–145 (2010).
44. Rigby, M. et al. Recent and future trends in synthetic greenhouse gas radiative forcing. *Geophys. Res. Lett.* **41**, 2623–2630 (2014).
45. Su, N.-Y. Development of baits for population management of subterranean termites. *Annu. Rev. Entomol.* **64**, 115–130 (2019).
46. Peterson, C., Wagner, T. L., Mulrooney, J. E. & Shelton, T. G. Subterranean Termites—Their Prevention and Control in Buildings. https://www.srs.fs.usda.gov/pubs/misc/misc_hg064.pdf (2006).
47. Pavley, F. & Nunez, F. AB-32 California Global Warming Solutions Act of 2006 (2006).
48. Pavley, F. & Garcia, E. SB-32 California Global Warming Solutions Act of 2016: emissions limit (2016).
49. California Air Resources Board. California Greenhouse Gas Emissions for 2000 to 2020: Trends of Emissions and Other Indicators. https://ww2.arb.ca.gov/sites/default/files/classic/cc/inventory/2000-2020_ghg_inventory_trends.pdf (2022).
50. California Air Resources Board. California Air Resources Board 2022 Scoping Plan for Achieving Carbon Neutrality. <https://ww2.arb.ca.gov/our-work/programs/ab-32-climate-change-scoping-plan/2022-scoping-plan-documents> (2022).
51. Calvert, G. M. et al. Health effects associated with sulfuryl fluoride and methyl bromide exposure among structural fumigation workers. *Am. J. Public Health* **88**, 1774–1780 (1998).
52. Schneir, A., Clark, R. F., Kene, M. & Betten, D. Systemic fluoride poisoning and death from inhalational exposure to sulfuryl fluoride. *Clin. Toxicol.* **46**, 850–854 (2008).
53. Harris, J., Kim, J., Lin, C., Stafford, D. & Weber, S. Report No. 17-P-0053 Additional Measures Can Be Taken to Prevent Deaths and Serious Injuries From Residential Fumigations. *U.S. Environmental Protection Agency, Office of Inspector General*. https://www.epa.gov/sites/default/files/2016-12/documents/_epaog_20161212-17-p-0053.pdf (2016).
54. Barreau, T., Hoshiko, S., Kreutzer, R., Smorodinsky, S. & Talarico, J. Sulfuryl fluoride poisonings in structural fumigation, a highly regulated industry—potential causes and solutions. *Int. J. Environ. Res. Public Health* **16**, 2026 (2019).
55. Appleyard, M. Sulfuryl Fluoride Draft Interim Re-Entry Mitigation Measures (Docket ID: EPA-HQ-OPP-2009-0163). <https://www.regulations.gov/document/EPA-HQ-OPP-2009-0136-0105> (2021).
56. Scheffrahn, R. H., Osbrink, W. L. A., Hsu, R. C. & Su, N. Y. Desorption of residual sulfuryl fluoride from structural and household commodities by headspace analysis using gas chromatography. *Bull. Environ. Contamination. Toxicol.* **39**, 769–775 (1987).
57. Scheffrahn, R. H., Bloomcamp, C. L. & Su, N.-Y. Indoor airborne residues of methyl bromide and sulfuryl fluoride following aeration of fumigated houses. *Indoor Air* **2**, 78–83 (1992).
58. Tao, J. Estimating sulfuryl fluoride emissions during structural fumigation of residential houses. *Water Air Soil Pollut.* **230**, 96 (2019).
59. California Air Resources Board. California Aeration Plan (CAP) for Structural Fumigations (2019).
60. Tratt, D. M., Buckland, K. N., Keim, E. R. & Hall, J. L. Identification and source attribution of halocarbon emitters with longwave-infrared spectral imaging. *Remote Sensing Environ.* **258**, 112398 (2021).
61. Buckland, K. N. et al. Tracking and quantification of gaseous chemical plumes from anthropogenic emission sources within the Los Angeles Basin. *Remote Sensing Environ.* **201**, 275–296 (2017).
62. United States Code. Clean Air Act, 42 U.S.C. §7401 et seq (1970).
63. Nie, Y. et al. Mass transfer and reaction kinetics of sulfuryl fluoride absorption with aqueous sodium hydroxide solutions. *J. Zhejiang Univ. Sci. A* **15**, 540–546 (2014).
64. Nie, Y. et al. Harmless treatment of sulfuryl fluoride by chemical absorption. *Environ. Eng. Sci.* **32**, 789–795 (2015).
65. Liang, X. et al. Solubility and thermodynamic properties of sulfuryl fluoride in water. *J. Chem. Thermodyn.* **95**, 190–194 (2016).
66. Liang, X. et al. Sulfuryl fluoride absorption from fumigation exhaust gas by biobased solvents: thermodynamic and quantum chemical analysis. *Indust. Eng. Chem. Res.* **58**, 5018–5029 (2019).
67. Andrews, A. E. et al. CO₂, CO, and CH₄ measurements from tall towers in the NOAA Earth System Research Laboratory's Global Greenhouse Gas Reference Network: instrumentation, uncertainty analysis, and recommendations for future high-accuracy greenhouse gas monitoring efforts. *Atmos. Meas. Tech.* **7**, 647–687 (2014).
68. Sweeney, C. et al. Seasonal climatology of CO₂ across North America from aircraft measurements in the NOAA/ESRL Global Greenhouse Gas Reference Network. *J. Geophys. Res.: Atmos.* **120**, 5155–5190 (2015).
69. Baier, B. C. et al. Multispecies assessment of factors influencing regional CO₂ and CH₄ enhancements during the winter 2017 ACT America campaign. *J. Geophys. Res.: Atmos.* **125**, e2019JD031339 (2020).
70. Davis, K. J. et al. The Atmospheric Carbon and Transport (ACT)—America Mission. *Bull. Am. Meteorol. Soc.* **102**, E1714–E1734 (2021).
71. Plant, G. et al. Large fugitive methane emissions from urban centers along the U.S. East Coast. *Geophys. Res. Lett.* **46**, 8500–8507 (2019).
72. Lin, J. C. et al. A near-field tool for simulating the upstream influence of atmospheric observations: The Stochastic Time-Inverted Lagrangian Transport (STILT) model. *J. Geophys. Res.* **108** (2003).
73. National Oceanic and Atmospheric Administration & National Centers for Environmental Information. North American Mesoscale Forecast System (NAM) [12 km]. <https://www.ncei.noaa.gov/metadata/geoportal/rest/metadata/item/gov.noaa.ncdc:C00630/html> (2004).

74. Nehrkorn, T. et al. Coupled weather research and forecasting-stochastic time-inverted lagrangian transport (WRF-STILT) model. *Meteorol. Atmos. Phys.* **107**, 51–64 (2010).
75. Fasoli, B., Lin, J. C., Bowling, D. R., Mitchell, L. & Mendoza, D. Simulating atmospheric tracer concentrations for spatially distributed receptors: updates to the Stochastic Time-Inverted Lagrangian Transport model's R interface (STILT-R version 2). *Geosci. Model Dev.* **11**, 2813–2824 (2018).
76. Karion, A. et al. Intercomparison of atmospheric trace gas dispersion models: Barnett Shale case study. *Atmos. Chem. Phys.* **19**, 2561–2576 (2019).
77. Gourdji, S. M. et al. Regional-scale geostatistical inverse modeling of North American CO₂ fluxes: a synthetic data study. *Atmos. Chem. Phys.* **10**, 6151–6167 (2010).
78. Miller, S. M., Michalak, A. M. & Levi, P. J. Atmospheric inverse modeling with known physical bounds: an example from trace gas emissions. *Geosci. Model Dev.* **7**, 303–315 (2014).
79. Feng, L. et al. Inter-annual variability in atmospheric transport complicates estimation of US methane emissions trends. *Geophysical Research Letters* **50**, e2022GL100366 (2023).
80. Michalak, A. M. et al. Maximum likelihood estimation of covariance parameters for Bayesian atmospheric trace gas surface flux inversions. *J. Geophys. Res.* **110**, D24107 (2005).
81. Fang, Y. & Michalak, A. M. Atmospheric observations inform CO₂ flux responses to environmental drivers. *Glob. Biogeochem. Cycles* **29**, 555–566 (2015).
82. Saibaba, A. K. & Kitanidis, P. K. Efficient methods for large-scale linear inversion using a geostatistical approach. *Water Resour. Res.* **48** (2012).
83. Saibaba, A. K. & Kitanidis, P. K. Fast computation of uncertainty quantification measures in the geostatistical approach to solve inverse problems. *Adv. Water Resour.* **82**, 124–138 (2015).

Acknowledgements

The authors thank Arlyn Andrews, Colm Sweeney, Phil Handley, Jack Higgs, Jon Kofler, Thomas Medford, Eric Moglia, Tim Newberger, and Sonja Wolter for their contributions to the NOAA GGGRN tower and aircraft flask programs, and we thank the LA Megacity program for facilitating collection of LAC air samples. We thank Chris Peterson, Thomas (Guy) Shelton, Vernard Lewis, Alan Stone, and Jared Leadbetter for insightful discussions on termite activity in the U.S. Funding for this work was provided by the National Science Foundation Environmental Engineering program grants #2121641 to Johns Hopkins University and #2121739 to the Scripps Institution of Oceanography at the University of California San Diego. This work was also supported by the National Oceanic and Atmospheric Administration Cooperative Agreement with the Cooperative Institute for Research in Environmental Sciences grant #NA17OAR4320101 and the National Oceanic and Atmospheric Administration Climate Program Office AC4 and COM program grants #NA21OAR4310233 and #NA21OAR4310234. Funding for the ECO aircraft campaign measurements

was provided by the National Oceanic and Atmospheric Administration Climate Program Office AC4 program grants #NA14OAR0110139 and #NA14OAR0110140. B.C.B. and ACT measurements were supported by National Aeronautics and Space Administration grant #NNX15AJ06G to the University of Colorado.

Author contributions

D.C.G. and S.M.M. designed research. D.C.G. performed research and created figures. D.C.G., J.M., L.H. and S.M.M. analyzed data. I.J.V., M.C., J.B.M., K.M., B.C.B. and B.R.M. collected and facilitated atmospheric measurements. M.Z. and J.B. provided modeling support. D.C.G., J.M. and S.M.M. wrote the paper with input from I.J.V., L.H., J.B.M., K.M., B.C.B. and M.Z.

Competing interests

The authors declare no competing interests.

Additional information

Supplementary information The online version contains supplementary material available at <https://doi.org/10.1038/s43247-024-01294-x>.

Correspondence and requests for materials should be addressed to Dylan C. Gaeta or Scot M. Miller.

Peer review information *Communications Earth & Environment* thanks Rudolf Scheffrahn and the other, anonymous, reviewer(s) for their contribution to the peer review of this work. Primary Handling Editors: Pallav Purohit and Clare Davis. A peer review file is available

Reprints and permissions information is available at <http://www.nature.com/reprints>

Publisher's note Springer Nature remains neutral with regard to jurisdictional claims in published maps and institutional affiliations.

Open Access This article is licensed under a Creative Commons Attribution 4.0 International License, which permits use, sharing, adaptation, distribution and reproduction in any medium or format, as long as you give appropriate credit to the original author(s) and the source, provide a link to the Creative Commons licence, and indicate if changes were made. The images or other third party material in this article are included in the article's Creative Commons licence, unless indicated otherwise in a credit line to the material. If material is not included in the article's Creative Commons licence and your intended use is not permitted by statutory regulation or exceeds the permitted use, you will need to obtain permission directly from the copyright holder. To view a copy of this licence, visit <http://creativecommons.org/licenses/by/4.0/>.

© The Author(s) 2024